Mn3MnNb2O9: high-pressure triple perovskite with 1:2 B-site order and modulated spins

COMMUNICATION

$Mn_3MnNb_2O_9$: high-pressure triple perovskite with 1:2 B-site order and modulated spins.

Received 00th January 20xx,
Accepted 00th January 20xx

DOI: 10.1039/x0xx00000x

Elena Solana-Madruga,*[a,b] Clemens Ritter,[c] Cintli Aguilar-Maldonado,[a] Olivier Mentré,[a] J. Paul Attfield[b] and Ángel M. Arévalo-López.*[a]

The first triple perovskite with Mn in A- and 1:2 B-site order $Mn_3MnNb_2O_9$, prepared by high pressure phase transformation of the magnetodielectric $Mn_4Nb_2O_9$, is reported herein. It has a complex magnetic behaviour with a transition from a collinear AFM into an evolving incommensurate spin density wave (SDW) further stabilised into a lock-in structure dictated by the B-site order.

ABO_3 materials with perovskite structure (Pv) are of great interest in the search for new compounds with enhanced properties. Pv accommodates a wide range of chemical compositions and possible cation order into both A and B sites.[1] Among these derivatives, several examples are known for 1:1 order into $AA'B_2O_6$ or $A_2BB'O_6$ double perovskites (DPv)[2] and more complex 1:3 order into $AA'_3B_4O_{12}$ quadruple perovskites (QPv).[3-5] However, 1:2 arrangements into $A_3BB'_2O_9$ triple perovskite (TPv) structures are not often observed.

The 1:2 TPv aristotype $Ba_3SrTa_2O_9$ crystallises with *P*-3*m*1 symmetry and $a = a_c\sqrt{2}$ and $c = a_c\sqrt{3}$ supercell ($a_c \approx 3.8$ Å for a cubic Pv).[6] Only examples with A = Ba, Sr, Ca and La are known [7] and they often present typical octahedrally tilted structures.[8,9] The related $A_3CoNb_2O_9$ TPvs show notable photocatalytic[10] and dielectric[11] properties, while $Ba_3BNb_2O_9$ (B^{2+} = Mn, Ni) TPvs are multiferroic materials.[12,13]

High pressure and high temperature (HPHT) synthesis method allows the stabilisation of the smaller Mn^{2+} cation into the A site of the Pv, giving rise to the so-called A-site manganites. These have attracted much attention in the search for new functional materials, providing accessibility to simple, double and quadruple perovskite derivatives, *e.g.* $Mn^{2+}V^{4+}O_3$-II,[14] $Mn^{2+}{}_2Fe^{3+}Re^{5+}O_6$[15] and $Mn^{2+}Mn^{3+}{}_3Mn^{3.25+}{}_4O_{12}$,[16] with a rich variety of physical properties.

In this article, we present the structure and properties of the first A-site manganite with $A_3BB'_2O_9$ TPv structure: HP-$Mn_3MnNb_2O_9$. The room pressure $Mn_4Nb_2O_9$ oxide has remarkable magnetoelectric properties[17] and a preliminary microscopy study of the high-pressure modification mentioned a distorted $a_m = \sqrt{2}\sqrt{3}a_c$, $b_m = \sqrt{2}a_c$ and $c_m = 2\sqrt{3}a_c$ monoclinic supercell, but no further studies have been performed.[18] HP-$Mn_3MnNb_2O_9$ TPv with a 1:2 Mn:Nb cation order shows a complex magnetic behaviour and we argue that the magnetic ground state is directly driven by the B-site cation ordering.

Rietveld fits against synchrotron (SXRD) and neutron powder diffraction (NPD) data collected at 300 and 100 K respectively (Fig. 1a and Tables 1 and S1) reveal a monoclinic structure with space group *Cc* and a = 9.9054(5) Å, b = 5.3097(2) Å, c = 13.2052(7) Å and β = 92.772(6) ° cell parameters for the NPD data, in agreement with the previous microscopy study.[18] The paraelectric *C2/c* symmetry was tested after reconstruction from the refined acentric one (with 3:1:5 Mn:Nb:O independent sites) but worse agreement factors were obtained (R_{WP} = 6.61% *C2/c vs*. 3.91% *Cc*). This model implies Mn3 to lie on a pseudo 2-fold axis, which is far away from the refined *Cc* model (see Fig. 1). The polar space group suggests the potential ferroelectricity of this material, which in combination with its complex magnetism makes it a possible multiferroic. The structure can be described as a distorted 1:2 Mn:Nb TPv with three independent Mn cations at the A-site generating the (002), (200) and (110) superstructure peaks labelled in Fig. 1a and detailed in Supplementary Fig. S1. Antisite mixing was tested but refining to ideal values within errors and thus fixed. M-O bond distances (Fig. 1c) confirm octahedral coordination for Nb and Mn2 on the B sites. Only six Mn2-O bonds are shorter than 3.5 Å (in the 1.89 – 2.33 Å range), while the same limit provides 10, 10 and 8-fold coordinations for Mn1, Mn3 and Mn4 respectively. The octahedra for the six different cations are schematised on Fig. 1c; their quadratic elongation (λ) and the bond angle variance (σ^2) with respect to an ideal octahedron of the same volume (Table 1) and their ratio (Fig. S2) show a much larger distortion for the A sites, supporting the 1:2 TPv structural description (HP-$Mn_3MnNb_2O_9$).[19]

HP-$Mn_3MnNb_2O_9$ shows an $a^-b^-c^-$ tilting system with large Φ_1 = 19.97 °, Φ_2 = 24.87 ° and Φ_3 = 15.80 ° tilt angles along *x*, *y* and *z* directions respectively (see Fig. S3), in agreement with the small A-site Mn^{2+} and comparable to other high-pressure A-site

[a] Univ. Lille, CNRS, Centrale Lille, ENSCL, Univ. Artois, UMR 8181 - UCCS - Unité de Catalyse et Chimie du Solide, F-59000 Lille, France.* elena.solanamadruga@univ-lille.fr and angel.arevalo-lopez@univ-lille.fr
[b] Centre for Science at Extreme Conditions (CSEC) and School of Chemistry, The University of Edinburgh. EH9 3FD, U.K.
[c] Institut Laue-Langevin, Avenue des Martyrs 71, 32042, Grenoble Cedex, France.
‡ Electronic Supplementary Information (ESI) available: supporting figures and tables. See DOI: 10.1039/x0xx00000x

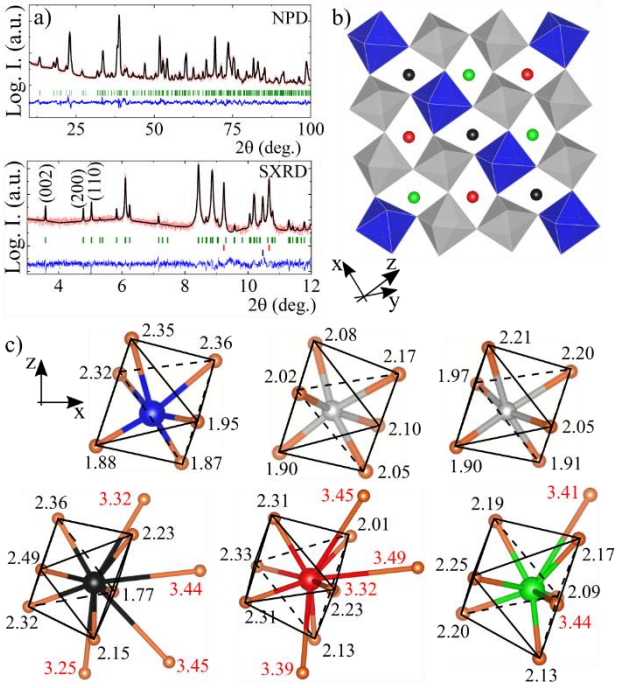

Figure 1. a) Rietveld fits against the NPD and SXRD data collected at 300 K for HP-$Mn_3MnNb_2O_9$ with (002), (200) and (110) superstructure peaks labelled for SXRD. Second and third rows of Bragg ticks are MnO and Pt from the capsule, only observed in the SXRD sample. b) One (11-2) layer of the refined structure, showing the 1:2 B-site order among Mn2 (blue) and Nb (grey) sites and the alternated Mn1 (black), Mn3 (red) and Mn4 (green) in A. c) coordination environments for each cation site, with schematised octahedral environments and longer Mn-O distances labelled in red.

Table 1. Atomic positions (all Wyckoff 4*a* sites fully occupied) of HP_$Mn_4Nb_2O_9$ as refined from 100 K high resolution NPD. Space group *Cc* and cell parameters *a* = 9.9054(5) Å, *b* = 5.3097(2) Å, *c* = 13.2052(7) Å and *β* = 92.772(6) °. Agreement factors: R_p = 2.97%, R_{wp} = 3.91 %, R_B = 6.96%, R_f = 5.83%, χ^2 = 6.75%.

Site	x	y	z
Mn1	0.735(3)	0.535(3)	0.420(2)
Mn2	0.448(3)	0.476(4)	0.463(2)
Mn3*	0.394	0.5	0.757
Mn4	0.558(3)	-0.002(5)	0.592(2)
Nb1	0.109(2)	0.508(3)	0.820(1)
Nb2	0.776(2)	0.492(3)	0.647(1)
O1	0.730(2)	0.698(2)	0.787(1)
O2	0.193(2)	0.687(2)	0.701(1)
O3	0.126(2)	0.870(2)	0.071(1)
O4	0.863(2)	0.334(2)	0.538(1)
O5	0.523(2)	0.663(2)	0.359(1)
O6	0.571(2)	0.191(2)	0.452(1)
O7	0.791(2)	0.844(2)	0.397(1)
O8	0.464(2)	0.893(2)	0.733(2)
O9	0.400(2)	0.291(2)	0.619(1)

	Mn1	Mn2	Mn3	Mn4	Nb1	Nb2
<λ>	1.088	1.036	1.059	1.054	1.012	1.018
$10^2\Delta$	0.79	1.12	2.94	1.57	0.51	1.21
σ^2 (deg^2)	243.70	86.35	181.05	172.75	36.47	50.39

Thermal factors constrained for stability of the refinements: $B_{iso}(M)$ = 0.22(6) Å^2, $B_{iso}(O)$ = 0.02(3) Å^2. *Mn3 site used as a cell reference. $\Delta = (1/6) * \sum(d_i-d_{av})^2/d_{av}$. $\langle\lambda\rangle = (1/6) * \sum(l_i/l_0)^2$ and $\sigma^2 = (1/11) * \sum(\theta_i-90^\circ)^2$.

manganites. Mn2 and Nb2 B-site octahedral distortions are considerably bigger than those observed in other 1:2 TPv and high pressure DPv A-site manganites;[11,20] HP-$Mn_3MnNb_2O_9$ distortion is only surpassed by the $MnMn_3Mn_4O_{12}$ QPv ($\langle\Delta\rangle$ = 16.5 deg^2 , $\langle 10^2\lambda\rangle_{Av}$ = 1.0295, $\langle\sigma^2\rangle$ = 80.22);[16] and thus, the "all transition metal" (ATM) HP-$Mn_3MnNb_2O_9$ is the first A-site Mn TPv and the second most distorted A-site manganite oxide up to date.

The coexistence of four independent Mn sites induces a complex magnetic behaviour with subsequent transitions observed in bulk magnetic susceptibility measurements at T_N = 52.1(1) K, T_M = 27.8(1) K and T_L = 4.2(1) K, as displayed in Fig.2, where *N*, *M* and *L* stand for Néel, modulated and lock-in respectively. The fit of the inverse susceptibility to the Curie-Weiss law above 125 K (Fig. S4) results in an effective magnetic moment of 5.92 μ_B/Mn, in good agreement with the expected value for Mn^{2+} d^5 cations, and a Weiss constant of ϑ = -334 K showing a large frustration index $f = |\vartheta|/T_N$ = 6.42. The three transitions are also observed in the magnetic contribution to the heat capacity shown in Fig.2. Integration of the three transitions from C_{mag}/T (Fig. S6a) reveal a total entropy release of 39(1) J/mol K, which is about 2/3 of the theoretical value S = 4*Rln(2S+1) = 59.59 J/mol K for HP-$Mn_3MnNb_2O_9$ (S = 5/2). Deconvolution of the entropy contributions (Fig. S6b) results in 59%, 39% and 2% for T_N, T_M and T_L respectively, suggesting a strong entropy release below T_N and T_M and even ordering of a fraction of the moments down to T_L as discussed below.

The temperature dependence of HP-$Mn_3MnNb_2O_9$ NPD data reveals the appearance of magnetic peaks below T_N = 52.1(1) K and their shift on cooling below T_M = 27.8(1) K (Fig. 3a). All magnetic peaks in the $T_M < T < T_N$ temperature range can be indexed with the propagation vector k_0 = [0 0 0]. The refined magnetic structure in this interval (R_{mag} = 14.0%) shows A-type AFM sublattices for all Mn sites (Fig. 3b) with spins aligned along the *c* axis and (101) AFM planes of Mn at the A-sites (dashed lines). All magnetic moments were constrained to the same values and refined to 2.68(1) μ_B.

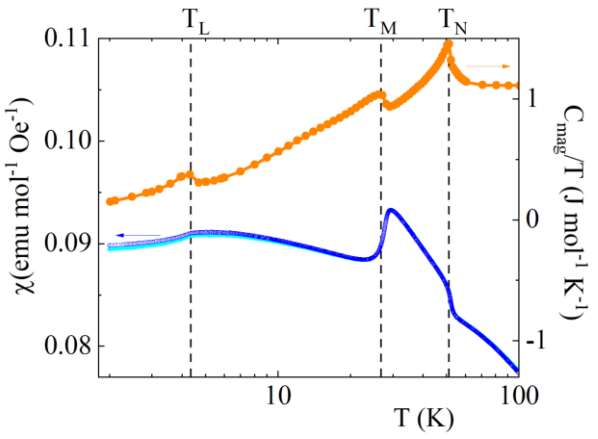

Figure 2. FC-ZFC magnetisation (blue, left axis) and magnetic contribution to the heat capacity (orange, right axis) of HP-$Mn_3MnNb_2O_9$. Transition temperatures are identified with vertical dashed lines.

Considering octahedral environments for all the Mn sites provides an understanding of the interactions involved (ESI): the dominant exchange is between face-shared Mn1-Mn2 octahedra and all MnA-MnB are AFM super-exchange in accordance with Goodenough-Kanamori-Anderson rules (GKA).[21] Thus, Mn2 is AFM to its nearest Mn1 but FM to Mn3 and Mn4, which involves a strong magnetic frustration and triggers the spin modulation observed below T_M.

Figure 3c shows the thermal behaviour of the propagation vector. Below T_M = 27.8(1) K, the abrupt displacements of the magnetic peaks follow a [k_x 0 k_z] propagation vector with the incommensurate components gradually evolving to k_x = 0.337(5) and k_z = -0.144(9) at 5 K and thus suggesting a lock-in transition to k_L = [⅓ 0 -⅙] at T_L = 4.2(1) K as shown by magnetisation and heat capacity measurements in Figure 2. Similar behaviours occur for instance in HP-Mn_2InSbO_6, which presents a continuous reorientation from k_0 into a lock-in transition to k = [0 0 ⅛].[22]

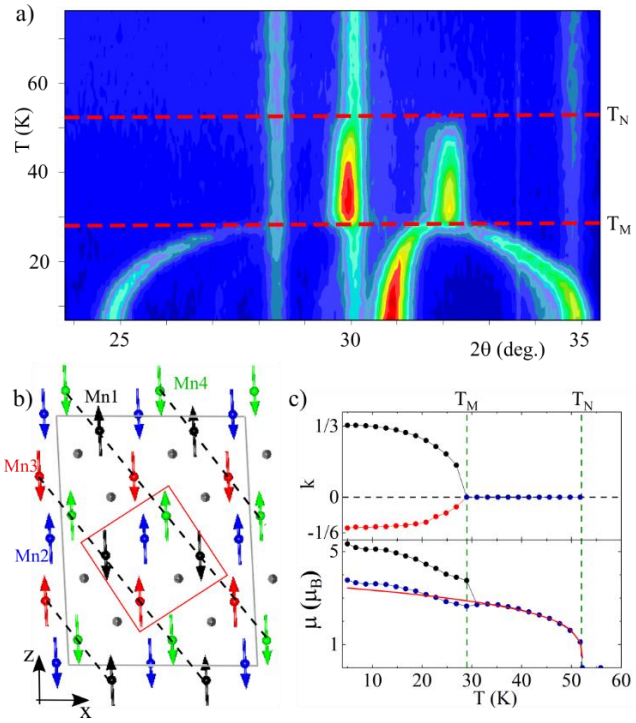

Figure 3. a) Thermal evolution of HP-$Mn_3MnNb_2O_9$ NPD data focused in the 24°-35° 2θ region. b) Magnetic structure at T_M < T < T_N, with k_0 = [0 0 0] and black, blue, red and green arrows representing the magnetic moments of Mn1 – Mn4 sites respectively. Grey spheres are Nb atoms. The red square highlights the frustrated (FM) blue-red and blue-green *vs.* dominant blue-black AFM interactions. Dashed lines show AFM A-site order. c) Refined magnetic propagation vector (top panel, k_x black and k_z red) and magnetic moment (bottom panel, maximum and averaged amplitudes in black and blue respectively) as a function of temperature. Vertical dashed lines mark T_N and T_M transition temperatures from magnetic susceptibility. Red line in bottom panel shows the fit to the critical law as detailed in the text.

The refined magnetic structure at 5 K (Fig. 4a) presents a sinusoidal modulation of the magnetic moments along *c*. An elliptical modulation of the magnetic moments is also physically possible; however, Rietveld fits against NPD at 5 K show that the simpler collinear SDW model gives better agreement R_{mag} factor (13% SDW *vs.* 15.5% elliptic model) and hence it is discussed here. The isotropic nature of Mn^{2+} single ion (d^5, L = 0) also supports the preferential alignment of the spins along the *c* axis in a SDW rather than their rotation into the plane via a poor influence of local orbital overlaps.

The k_0 structure minimises its exchange energy between unfavourable FM spins by modulating the magnetic moments between 0 and a maximum amplitude of 5.1(1) μ_B at 5 K. The thermal evolution of the magnetic moments, Figure 3c, shows a coherent increase of the averaged moment, calculated as $\mu_{max}/\sqrt{2}$. The averaged ordered moment magnitude at 5 K of 3.6(1) μ_B is 72% of the ideal value, so one-third of the spins remain dynamic below the magnetic ordering transitions, consistent with the persistence of 1/3 of the theoretical magnetic entropy. The fit of the saturated moment in the k_0 region using a critical law $\mu = \mu_0 * (1- (T/T_N))^{\beta}$ results in μ_0 = 3.52(8) μ_B, T_N = 52.2(2) K and β = 0.25(1). The critical exponent β is intermediate between 2D and 3D systems, the former only ordering in the Ising case. Therefore, the 2D-lattice in the *ab* plane would predominate but order via weaker interplane exchanges.

2D models are reported for related $A_3BNb_2O_9$ 1:2 TPv with non-magnetic A-site cations.[12,13] There, completely isolated triangular lattice antiferromagnets (TLAFs) with the spins confined to the *ab* plane are stacked along the *c* axis. Here, the presence of 75% of the magnetic cations in the A-site defines the magnetic backbone of HP-$Mn_3MnNb_2O_9$ but the sole presence of one magnetic cation in three in the B lattice enables the A-B frustrated interactions and finally destabilizes the k_0 structure at k_M and below.

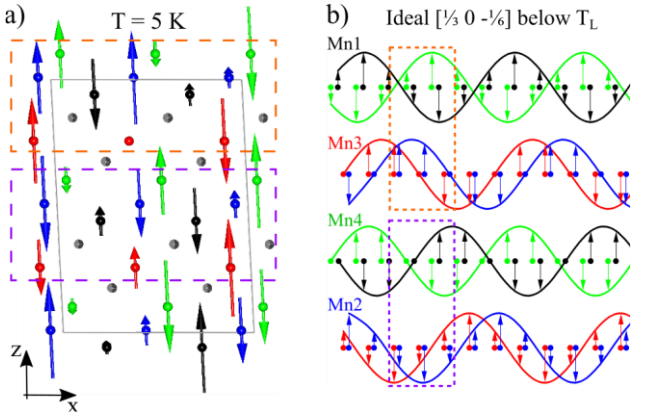

Figure 4. a) Magnetic structure at 5 K with k = [k_x 0 k_z]. Orange and purple dashed rectangles mark 2D-like blocks separated by Nb. b) Ideal magnetic structure with k_L = [⅓ 0 -⅙] showing the alternated sinusoidal and UU0DD0 chains of each magnetic site along the z axis. One unit cell is identified for each block using the orange and purple dashed rectangles.

The SDW described by all Mn sites are schematised in Fig. 4b for the ideal k_L = [⅓ 0 -⅙] model below T_L. They describe two different types of waves propagating along *a* and alternating along *c*: i) sinusoidal waves with 3 modulated spins up and 3 down and ii) 2 up-null-2 down-null patterns (UU0DD0). The nearly identical phase refined for AFM Mn1 and Mn4 sites at 5 K is reflected in the similar behaviour of their waves, which are coupled in Fig 4b for simplicity. Mn2 and Mn3 waves are almost FM coupled.

Collinearly ordered components with full amplitude modulation within a SDW is very rare in oxides. The only closely related systems we are aware of where the collinear moments of spin chains are fully modulated are $MnVO_3$,[14] $NaYNiWO_6$,[23, 24] $Ca_3Co_2O_6$[25] and Fe_2GeO_4.[26] the two later cases are for S = 2 $3d^6$ ions with unquenched orbital contributions for the cobalt case. Among all the Pv-type A-site manganites only $MnVO_3$ (k = [0.29 0 0]),[14] Mn_2FeSbO_6 (k = [0 0.43 0])[25] and $MnMn_3Mn_4O_{12}$ (k = [0 0 k_z])[28,29] show incommensurate propagation vectors while HP-$Mn_3MnNb_2O_9$ exhibits a bidirectional k_M = [k_x 0 k_z] one. As $MnVO_3$, HP-$Mn_3MnNb_2O_9$ shows S = 5/2 Mn^{2+} with no orbital degeneracy and thus minimises its exchange energy by retaining fluctuating moment components below T_L. As detailed in ESI, a hypothetical situation with fully saturated Mn moments for the k_0 phase would have an energy of E_f = 150**J*. Instead, the energy associated with the SDW results in $E_f(k_L)$ = 65.40**J*. Therefore, a clear benefit is obtained from the modulation, while part of the magnetic moments saturates to their ideal 2*S* = 5 μ_B value.

Non-magnetic A-site 1:2 TPv propagation vectors related to the triangular B-site lattice are usually observed, *e.g.* [⅓ ⅓ 0] or [⅓ ⅓ ½].[12,13] The presence of the A-site manganese in HP-$Mn_3MnNb_2O_9$ dictates the AFM k_0 structure. However, the underlying 1:2 B-site ordering stablishes the frustration via A-B interactions and thus the leitmotiv of the triangular lattice remains, eventually inducing the modulation and the lock-in ground state.

In conclusion, the discovery of HP-$Mn_3MnNb_2O_9$ TPv closes the gap between the known types of cation ordered A-site manganites. HP- $Mn_3MnNb_2O_9$ shows a full 1:2 Mn:Nb cation order and is also the second most distorted A-site manganite oxide up to date. It presents a simultaneous order of the four independent Mn cations with a simple but highly frustrated k_0 magnetic structure. The structure minimises the frustration between unfavourably oriented spins via large amplitude modulations and stabilises in a lock-in structure with k_L = [⅓ 0 -⅙] directly related to the 1:2 cation order.

Acknowledgments

We thank EPSRC for support, and ALBA and the ILL for beamtime provided at BL04 and D20 (doi:10.5291/ILL-DATA.5-31-2674) beamlines respectively. Alexandr Missiul is acknowledged for assistance on ALBA data collection. AMAL thanks the ANR-AMANTS project (19-CE08-0002-01). CAM thanks CONACyT-Mexico for a post-doctoral fellowship (CVU 350841). Chevreul Institute (FR 2638), Region Hauts-de-France, and FEDER are acknowledged for funding the X-ray diffractometers and the PPMS magnetometer.

Notes and references

[1] S. Vasala, M. Karppinen. *Prog. Solid State Chem.* **2015**, *43*, 1– 36.
[2] G. King, P. M. Woodward. *J. Mater. Chem.* **2010**, *20*, 5785– 5796.
[3] A. Prodi, E. Gilioli, A. Gauzzi, F. Licci, M. Marezio, F. Bolzoni, Q. Huang, A. Santoro, J. W. Lin, *Nat. Mater.* **2004**, *3*, 48.-52.
[4] a) N. J. Perks, R. D. Johnson, C. Martin, L.C. Chapon, P.G. Radaelli, *Nat. Commun.,* **2012**, *3*, 1-6. b) R. D. Johnson, D. D. Khalyavin, P. G. Radaelli, C. Martin, *Phys. Rev. Lett.*, **2012**, *108*, 067201.
[5] W.-T. Chen, M. Mizumaki, H. Seki, M. S. Senn, T. Saito, D. Kan, J. P. Attfield, Y. Shimakawa. *Nat. Commun.* **2014**, *5*, 3909.
[6] F. Galasso, L. Katz, *J. Am. Chem. Soc.* **1961**, *83*, 13, 2830–2832.
[7] P. K. Davies, H. Wu, A. Y. Borisevich, I. E. Molodetsky, L. Farber, *Annu. Rev. Mater. Res.* **2008**, *38*, 369-401.
[8] C. J. Howard, H. T. Stokes, *Acta Cryst.* **2004**, *B60*, 674-684.
[9] R. H. Mitchell. *Perovskites: modern and ancient.* Almaz Press Inc. Ontario, Canada, **2002**, pp. 89-91.
[10] V. Ting, Y. Liu, R.L. Withers L. Norén, *J. Solid State Chem.*, **2004**, *177*, 2295-2304.
[11] V. Ting, Y. Liu, L. Norén, R.L. Withers, D.J. Goossens, M. James, C. Ferraris, *J. Solid State Chem.*, **2004**, *177*, 4428-4442.
[12] M. Lee, E. S. Choi, X. Huang, J. Ma, C. R. Dela Cruz, M. Matsuda, W. Tian, Z. L. Dun, S. Dong, H. D. Zhou, *Phys. Rev. B,* **2014**, *90*, 224402.
[13] J. Hwang, E. S. Choi, F. Ye, C. R. Dela Cruz, Y. Xin, H. D. Zhou, P. Schlottmann, *Phys. Rev, Lett.* **2012**, *109*, 257205.
[14] M. Markkula, A. M. Arevalo-Lopez, A. Kusmartseva, J. A. Rodgers, C. Ritter, H. Wu, J. P. Attfield. *Phys. Rev. B*, **2011**, *84*, 094450.
[15] a) A.M. Arévalo-López, G.M. McNally, J.P. Attfield, *Angew. Chem. Int. Ed.* **2015**, *54*, 12074-12077. b) M.R. Li, M. Retuerto, Z. Deng, P.W. Stephens, M. Croft, Q. Huang, H. Wu, X. Deng, G. Kotliar, J. Sánchez-Benítez, J. Hadermann, D. Walker, M. Greenblatt, *Angew. Chem. Int. Ed.* **2015**, *54*, 12069-12073.
[16] S. V. Ovsyannikov, A. M. Abakumov, A. A. Tsirlin, W. Schnelle, R. Egoavil, J. Verbeeck, G. Van Tendeloo, K. V. Glazyrin, M. Hanfland, L. Dubrovinsky. *Angew. Chem. Int. Ed.* **2013**, *52*, 1494-1498.
[17] Y. Fang, W. P. Zhou, S. M. Yan, R. Bai, Z. H. Qian, Q. Y. Xu, D. H. Wang, Y. W. Du, *J. Appl. Phys.* **2015**,*117*, 17B712.
[18] A. P. Tyutyunnik, V. G. Zubkov, Y. G. Zainulin, N. V. Tarakina, M. J. Sayagués, G. Svensson, *Solid State Sciences*, **2002**, *4*, 941-949.
[19] K. Robinson, G. V. Gibbs, P. H. Ribbe, Science **1971**, *172*, 567-570.]
[20] Á. M. Arévalo-López, E. Solana-Madruga, C. Aguilar-Maldonado, C. Ritter, O. Mentré, J. P. Attfield, *Chem. Commun.* **2019**, *55*, 14470
[21] J. B. Goodenough. *Magnetism and the Chemical Bond*, New Wiley, New York, **1963**, pp. 180-181.
[22] Á. M. Arévalo-López, E. Solana-Madruga, E. P. Arévalo-López, D. Khalyavin, M. Kepa, A. J. Dos santos-García, R. Sáez-Puche, J. P. Attfield, *Phys. Rev. B,* **2018**, *98*, 214403.
[23] R. Shankar, F. Orlandi, P. Manuel, W. Zhang, P. S. Halasyamani, A. Sundaresan, *Chem. Mater.* **2020**, *32, 5641-5649.*
[24] H.-J. Koo, R. Shankar, F. Orlandi, A. Sundaresan, M.H. Whangbo, *Inorg. Chem.* **2020***, 59, 17856-17859.*
[25] S. Agrestini, L. C. Chapon, A. Daoud-Aladine, J. Schefer, C. Mazzoli, M. R. Lees, O. A. Petrenko, *Phys. Rev. Lett.* **2008**, *101*, 097207.
[26] G. Perversi, A. M. Arevalo-Lopez, C. Ritter, J. P. Attfield, Comm. Phys. **2018**, *1*, 69.
[27] A. J. Dos santos-García, C. Ritter, E. Solana-Madruga, R. Sáez-Puche, *J. Phys.: Condens. Matter*, **2013**, *25*, 206004.
[28] D. D. Khalyavin, R. D. Johnson, P. Manuel, A. A. Tsirlin, A. M. Abakumov, D. P. Kozlenko, Y. Sun, L. Dubrovinsky, S. V. Ovsyannikov, *Phys. Rev. B,* **2018**, *98*, 014426.
[29] J. Cong, K. Zhai, Y. Chai, D. Shang, D. D. Khalyavin, R. D. Johnson, D. P. Kozlenko, S. E. Kichanov, A. M. Abakumov, A. A. Tsirlin, L. Dubrovinsky, X. Xu, Z. Sheng, S. V. Ovsyannikov, Y. Sun, *Nat. Commun.* **2018**, *9*, 2996.

